Journal of Materials Chemistry A

ROYAL SOCIETY OF CHEMISTRY

PAPER

View Article Online
View Journal | View Issue

Cite this: J. Mater. Chem. A, 2021, 9, 27019

Gas adsorption in the topologically disordered Fe-BTC framework†

Adam F. Sapnik, [a] Christopher W. Ashling, [a] Lauren K. Macreadie, [bc] Seok J. Lee, [b] Timothy Johnson, [d] Shane G. Telfer [b] and Thomas D. Bennett *[a]

Received 29th September 2021
Accepted 19th November 2021

DOI: 10.1039/d1ta08449f

rsc.li/materials-a

Disordered metal–organic frameworks are emerging as an attractive class of functional materials, however their applications in gas storage and separation have yet to be fully explored. Here, we investigate gas adsorption in the topologically disordered Fe-BTC framework and its crystalline counterpart, MIL-100. Despite their similar chemistry and local structure, they exhibit very different sorption behaviour towards a range gases. Virial analysis reveals that Fe-BTC has enhanced interaction strength with guest molecules compared to MIL-100. Most notably, we observe striking discrimination between the adsorption of C_3H_6 and C_3H_8 in Fe-BTC, with over a twofold increase in the amount of C_3H_6 being adsorbed than C_3H_8. Thermodynamic selectivity towards a range of industrially relevant binary mixtures is probed using ideal adsorbed solution theory. Together, this suggests the disordered material may possess powerful separation capabilities that are rare even amongst crystalline frameworks.

Introduction

Metal–organic frameworks (MOFs) are hybrid materials known for their chemical and structural diversity.[1] With surface areas reported in excess of 7000 $m^2\ g^{-1}$, they are emerging as promising candidates for gas storage.[2,3] Furthermore, their pore architectures, tuneable between 3 and 100 Å in diameter, are well suited for various separation processes, such as industrial gases and hydrocarbons.[4–10]

MOFs are capable of gas separation through thermodynamic, kinetic, molecular sieving, and even quantum effects.[11] Separation depends on many properties of the framework; surface area, pore size, surface chemistry, the presence of functional groups, unsaturated metal sites, extra-framework ions and water molecules.[5] The kinetic diameter, polarizability and permanent polarity of the guest also play an important role, complicating the prediction of porous material's separation capabilities prior to measuring adsorption isotherms.

The separation of industrial gases, specifically the capture of CO_2 from CO_2/N_2 or CO_2/CH_4 mixtures, is increasing in importance given the environmental impact of the rising global greenhouse gas emissions.[12] Another key area is the petrochemical industry, which relies on the separation of hydrocarbons for use as fuels and chemical feedstocks for the production of polymers.[7] Separation of hydrocarbons of the same chain length is not easily achieved given their similar physical properties. For example, the boiling points of C_2H_4 and C_2H_6 differ by 15 K, while for C_3H_6 and C_3H_8 the difference is only 5 K.[13] Coupled with a molecular size difference of less than 0.4 Å, C_3H_6/C_3H_8 separation is a very challenging and extremely energy-intensive process.[7]

Very few crystalline MOFs have been found to successfully discriminate between the two gases. Developing MOFs for these applications requires consideration of not only the selectivity itself but also the chemical stability, recyclability, handling stability and capacity of the material, which are all important for practical use within an industrial setting.[14,15] MOFs are particularly attractive candidates due to the intricate ways in which their pore architecture and surface chemistry can be modified to tune the interactions with guest molecules.[16]

MIL-100 is a crystalline MOF, comprising Fe(III) centres and 1,3,5-benzenetricarboxylate linkers, arranged into oxo-centred trimer motifs that further assemble into hybrid tetrahedra [Fig. 1a and b].[17] Its hierarchical structure has a specific surface area in excess of 2000 $m^2\ g^{-1}$ and contains two types of mesopore with internal diameters of 25 and 29 Å, accessible through 5.5 and 8.6 Å apertures, respectively [Fig. 1c]. The crystallographic unit cell has a cell volume in excess of 390 000 $Å^3$ [Fig. 1d].

Activation of MIL-100 at temperatures below 150 °C generates coordinatively unsaturated Fe(III) sites, while temperatures above 150 °C induce partial reduction to form unsaturated Fe(II) sites, which may lead to enhanced interactions with certain

[a]Department of Materials Science and Metallurgy, University of Cambridge, Cambridge, CB3 0F2, UK. E-mail: tdb35@cam.ac.uk

[b]MacDiarmid Institute for Advanced Materials and Nanotechnology, Institute of Fundamental Sciences, Massey University, Palmerston North, New Zealand

[c]School of Chemistry, University of Sydney, Sydney, NSW, 2006, Australia

[d]Johnson Matthey Technology Centre, Blount's Court, Sonning Common, RG4 9NH, UK

† Electronic supplementary information (ESI) available. See DOI: 10.1039/d1ta08449f

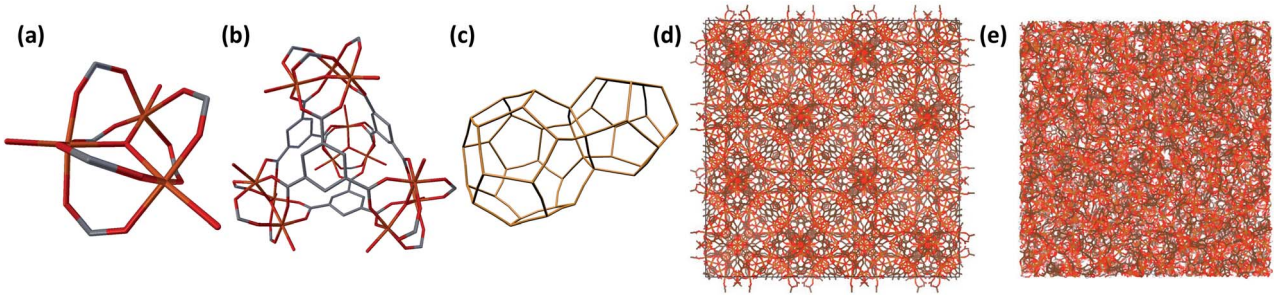

Fig. 1 (a) Oxo-centred trimer unit. (b) Hybrid tetrahedral assembly of trimers. (c) Net of the **mtn** topology framework. (d) Crystallographic unit cell of MIL-100 viewed along the *c* axis. (e) Representative model of the disordered Fe-BTC structure. Fe (orange), O (red), C (grey), H omitted for clarity. Figures adapted from ref. 29 and 33.

adsorbates.[18] These unsaturated metal sites are effective in aiding the separation of light hydrocarbons, with interaction strengths following the order $C_2H_2 > C_2H_4 > C_2H_6 > CH_4$.[19] A similar increase in interaction strength was observed between MIL-100 and C_3H_6 compared to C_3H_8 upon generation of the unsaturated Fe(II) sites, which can donate electron density to the π^* orbital of the alkene. This enhances the metal–adsorbate interaction strength and suggests the potential for C_3H_6/C_3H_8 separation in MIL-100 when activated above 150 °C.[20] MIL-100 has also found applications in water harvesting and as a Friedel–Crafts reaction catalyst.[21]

Amorphous MOFs share the local structure of their crystalline counterparts but lack any long-range order.[22,23] Typically, they are obtained *via* the collapse of a crystalline material through the application of heat or pressure. Structural disorder within MOFs has been demonstrated to improve conductivity, mechanical response, and mass transfer capacity compared to crystalline frameworks.[24] Notable examples of amorphous MOFs are found within the zeolitic imidazolate framework (ZIF) family, such as the hybrid glass a_gZIF-62 [$Zn(Im)_2(bIm)_{2-x}$; Im – imidazolate, bIm – benzimidazolate; a_g denoting the glass state], which is obtained through the melt-quenching of crystalline ZIF-62.[25] Recently, mechanical amorphisation of ZIF-8 [$Zn(mIm)_2$; mIm – 2-methylimidazolate], to form a_mZIF-8 (a_m denoting amorphisation by ball milling), was found to enhance the adsorption selectivity of C_3H_6 over C_3H_8.[26,27] Despite this, investigations into disordered MOFs for applications in gas storage and separation are of comparatively low prevalence with respect to their crystalline counterparts, particularly in the area of C_3H_6/C_3H_8 separation.

Fe-BTC, known commercially as Basolite® F300, has the same chemical composition as MIL-100 and is topologically disordered, lacking long-range order [Fig. 1e].[28,29] X-ray absorption near edge structure analysis of Fe-BTC revealed the presence of octahedrally coordinated Fe(III) ions at ambient temperature.[30] Furthermore, analysis of the extended X-ray absorption fine structure region revealed Fe-BTC possessed the same trimer unit structure present in MIL-100. Synchrotron X-ray pair distribution function analysis revealed the presence of mixed hierarchical local structure within Fe-BTC, confirming the trimer unit's existence and the presence of tetrahedral assemblies as observed in MIL-100.[29] This characterisation was used to produce the first atomic-scale model of Fe-BTC.

Upon activation at 120 °C, removal of water molecules coordinated to the Fe(III) ions in the trimer unit leads to the formation of coordinatively unsaturated metal sites.[30] This causes a lowering of the octahedral symmetry but does not induce the structural rearrangement of the framework. Upon activation at the slightly higher temperature of 150 °C, a small proportion of unsaturated Fe(II) sites were detected using NO-probed infrared spectroscopy in Fe-BTC and MIL-100.[31] At this temperature, the concentration of Lewis acid sites was estimated to be 40 and 30% for MIL-100 and Fe-BTC, respectively. At 250 °C the proportion of Fe(II) sites was greater in MIL-100 than Fe-BTC; beyond this temperature, Fe-BTC began to show signs of decomposition. Fe-BTC has been studied for its catalytic ability and outperforms MIL-100 in Lewis acid catalysis.[32] This has been attributed to its unsaturated metal sites and additional Brønsted acid sites, which are likely to influence its interactions with guest molecules.[31,33]

The morphological and porous nature of Fe-BTC is highly synthesis dependent. Often obtained *via* a sol–gel route, the Fe-BTC gel can subsequently be dried (i) through exchange with supercritical CO_2 (sCO_2) to obtain hierarchically porous aerogels, (ii) at room temperature for several days to afford xerogels, or (iii) at higher temperatures overnight to produce powdered samples.[28] The use of sCO_2 exchange avoids destructive capillary forces, which cause the collapse of the hierarchically porous architecture. Aerogel samples of Fe-BTC possessed a total pore volume of 5.62 $cm^3\ g^{-1}$ and a single point Brunauer–Emmett–Teller (BET) surface area of 1618 $m^2\ g^{-1}$. Xerogel samples had a BET surface area of around 800 $m^2\ g^{-1}$ that could be increased to 1182 $m^2\ g^{-1}$, with a total pore volume of 0.71 $cm^3\ g^{-1}$, through the ageing of the gel before drying. The powdered sample of Fe-BTC was least porous but was easiest to prepare. Quenched solid density functional theory analysis of the N_2 adsorption isotherm revealed that the xerogel had a broad pore size distribution in both the micro- and mesopore range up to 4.5 nm with maxima at 1.3 and 3.0 nm. The aerogel contained an even broader distribution in the whole range of micro- and mesopores with the same maximum at 1.3 nm.[28]

More recent investigations, using the harsher drying conditions employed in this study, gave rise to powdered Fe-BTC

samples that were essentially non-porous to nitrogen at 77 K, yet still retained the same local structure as MIL-100.[29] Basolite® F300, whose exact synthetic route remains undisclosed, has a BET surface area in the range 1300 to 1600 $m^2 g^{-1}$ as reported by the manufacturers. Independent experimental measurements have reported the BET surface area to be around 685 to 840 $m^2 g^{-1}$, with a total pore volume of 0.29 $cm^3 g^{-1}$ and pore size of 2.2 nm.[31,34]

Computational modelling has suggested that the degree of tetrahedral assembly in Fe-BTC materials influences the porosity, with accessible surface area increasing with the proportion of tetrahedral assemblies.[29] One atomic-scale model of Fe-BTC, for example, contained appreciable internal porosity while remaining non-porous to a nitrogen-sized probe. This model demonstrated the successful percolation of a 3.19 Å diameter spherical probe through the structure and revealed a maximum spherical cavity size of 9.15 Å. This analysis was performed from a purely geometric perspective and did not consider dynamics within the real material. Nonetheless, this suggests that Fe-BTC may have adsorption capacity for other gases given the dynamic nature of the material under realistic conditions.

Given the existing promise of MIL-100 in gas sorption and separation, the absence of long-range order in Fe-BTC means it is well placed to explore how topological disorder affects sorption and selectivity in MOFs. The area of C_3H_6/C_3H_8 separation is particularly interesting, given the limited number of crystalline MOFs reported with this behaviour. Ultimately, we aim to demonstrate the importance of disorder as a tool to augment and enhance properties of MOFs in the field of gas sorption and separation.

Experimental methods

Materials

All chemicals were obtained from commercial suppliers and used as received. Iron(III) nitrate nonahydrate (99.95%), 1,3,5-benzenetricarboxylic acid (95%), methanol (99.8%), ethanol (99.8%), ammonium fluoride (99.99%), sodium hydroxide pellets (98%) and iron(II) chloride tetrahydrate (99.99%) were all purchased from Sigma Aldrich. Ultrahigh purity gases were used as received from BOC gases.

Synthesis

MIL-100. MIL-100, $Fe_3(OH)(H_2O)_2O[(C_6H_3)(CO_2)_3]_2 \cdot nH_2O$, was synthesised following the procedure in ref. 35. 1,3,5-Benzenetricarboxylic acid (1.676 g), dissolved in 1 M aqueous sodium hydroxide (23.72 g), was added dropwise to a solution of iron(II) chloride tetrahydrate (2.260 g) dissolved separately in water (97.2 mL). The green suspension was left to stir at room temperature for 24 hours. The product was recovered by centrifugation, washed thoroughly with ethanol (3 × 20 mL), and dried overnight at 60 °C. The orange powder was purified following ref. 36. Briefly, the powder was dispersed and heated for 3 hours in each water (700 mL at 70 °C), ethanol (700 mL at 65 °C) and 38 mM aqueous ammonium fluoride solution (700 mL at 70 °C). The powder was recovered between each stage by centrifugation. The final product was dried overnight at 60 °C.

Fe-BTC. Fe-BTC was synthesised following the procedure in ref. 29. Both iron(III) nitrate nonahydrate (2.599 g) and 1,3,5-benzenetricarboxylic acid (1.177 g) were dissolved in methanol (20 mL each). The two solutions were combined at room temperature and left to stir for 24 hours, forming a viscous orange solution. This was washed with ethanol (3 × 20 mL) before drying overnight at 60 °C. The powder was then purified as described above and left to dry overnight at 60 °C.

Powder X-ray diffraction

Powder X-ray diffraction data were collected at room temperature using a Bruker D8 diffractometer using Cu $K_{\alpha 1}$ (λ = 1.5406 Å) radiation and a LynxEye position-sensitive detector with Bragg–Brentano parafocusing geometry. Samples of finely ground powder were dispersed onto low-background silicon substrates and loaded onto the rotating stage of the diffractometer. Data were collected over the angular range $2^\circ < 2\theta < 50^\circ$. Pawley refinements were carried out using TOPAS Academic (V6) software.[37] The unit cell parameters were refined against those previously reported for MIL-100.[17] A modified Thompson–Cox–Hasting pseudo-Voigt peak shape and simple axial divergence correction were employed.

Gas sorption

Gas adsorption isotherms and kinetic profiles were measured using a Quantachrome iQ2 instrument. Prior to measurement, samples were degassed at 150 °C for 12 hours. Sample masses were measured using degassed samples after the sample tube was backfilled with N_2. Sample temperatures were accurately equilibrated at 273 K and 293 K using a temperature-controlled water bath and at 77 K using a Dewar filled with liquid N_2. Under these conditions, MIL-100 and Fe-BTC are expected to contain coordinatively unsaturated Fe(III) sites with little to no partial reduction to Fe(II) occurring.[31] See ESI† Methods for details on the surface area, non-local density functional theory, virial, and ideal adsorbed solution theory analyses.

Results and discussion

Structural characterisation and nitrogen adsorption

Samples of MIL-100 and Fe-BTC were prepared following previously reported procedures (see Experimental methods for details). Powder X-ray diffraction measurements confirmed the crystalline nature and phase purity of MIL-100 [Fig. 2, S1, and Table S1†]. The diffraction pattern for Fe-BTC did not contain sharp Bragg scattering. Instead, broad regions of weak scattering were observed, consistent with its lack of long-range order yet possession of trimer-based local structure similar to that present in MIL-100.[29] We have previously reported on the morphologies of MIL-100 and Fe-BTC, as studied here, in ref. 29. MIL-100 contained 20 μm aggregates of sub 1 μm particles with some degree of faceting and Fe-BTC contained 20 μm fragments studded with 200 nm particles. It was not possible to

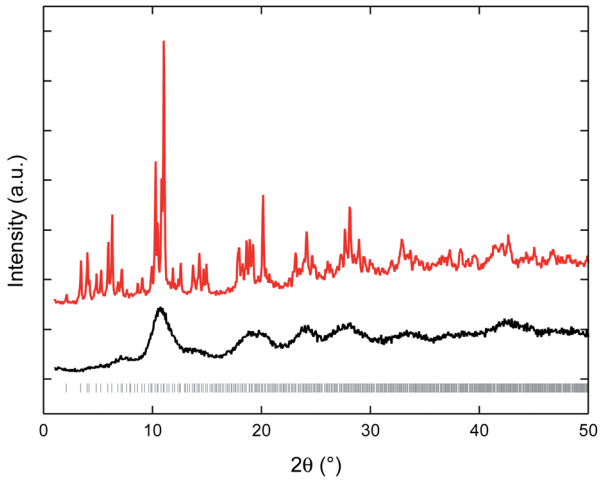

Fig. 2 Powder X-ray diffraction data for MIL-100 (red) and Fe-BTC (black), symmetry-allowed reflections for MIL-100 are shown as grey tick marks. Data reproduced from ref. 29.

determine the exact morphology of the particles in either material.

The N_2 adsorption isotherm for MIL-100 at 77 K displayed the expected intermediate Type I and IV behaviour indicative of the presence of both micro- and mesopores with a secondary uptake at approximately 0.12 P/P_0, a signature of the dual-pore architecture [Fig. 3].[17] The BET surface area was 1465 $m^2\ g^{-1}$, with a maximal uptake of 479.4 $cm^3\ g^{-1}$ [Table S2†]. Fe-BTC, however, exhibited an almost negligible maximal uptake of 42.1 $cm^3\ g^{-1}$ and hence the BET surface area (68 $m^2\ g^{-1}$) cannot readily be regarded as reliable.

Non-local density functional theory can be used to extract the pore size distribution from an adsorption isotherm [Fig. S2 and S3†]. This approach can be informative, despite the limitations discussed in the ESI Methods.† The pore size distribution for MIL-100 had maxima at 9.5 and 16.9 Å, while Fe-BTC possessed maxima at 9.1 and 17.3 Å [Fig. S4 and S5†]. The pores in Fe-BTC were present in a significantly lower amount than in MIL-100, hence the lower porosity of Fe-BTC. Notably, the contribution of the larger pore cavity was appreciably less in Fe-BTC than in MIL-100, suggesting the porous interior of Fe-BTC is largely comprised of the smaller pore structure. This pore cavity has a smaller crystallographic window aperture of 5.5 Å (*cf.* 8.6 Å aperture in the larger pore). It is the ordered network structure of MIL-100 that facilitates uptake and diffusion of guest molecules through the pores and connected apertures. In contrast, the topologically disordered nature of Fe-BTC disrupts the accessibility of the pores and results in a decrease in accessible surface area towards N_2 at this temperature. This has also been observed in ZIFs and their melt-quenched glass counterparts.[38]

These results suggest that the porous interior of Fe-BTC is inaccessible to N_2 at 77 K. Measurement of the N_2 isotherms at 273 K revealed that Fe-BTC is not a dense, non-porous material [Fig. S6†]. At 77 K there is an 11-fold decrease in the maximal uptake of N_2 in Fe-BTC compared to MIL-100. Whereas at 273 K this is greatly reduced to a factor of only 1.4. This is symptomatic of activated diffusion, where N_2 molecules cannot successfully diffuse through Fe-BTC at 77 K but can overcome this energetic barrier at higher temperatures.[39] Motivated by this, we further investigated the porous nature of these two materials by measuring a series of gas sorption isotherms (H_2, CO_2, Xe, Ar, CH_4, C_2H_4, C_2H_6, C_3H_6 and C_3H_8) at 77, 273 or 293 K up to 100 kPa [see Table S3† for analyte properties].

Hydrogen and carbon dioxide

Pure isotherms of H_2 were measured at 77 K for MIL-100 and Fe-BTC [Fig. 4]. The initial uptake was similar in both materials up to 20 kPa, exhibiting rapid adsorption kinetics.[40] The H_2 isotherms deviate at higher pressure where the larger surface area of MIL-100 allows for greater uptake of H_2. At the highest pressure, the maximal uptake of MIL-100 was 110.7 $cm^3\ g^{-1}$, and 74.7 $cm^3\ g^{-1}$ for Fe-BTC, though neither isotherm reached saturation at the pressures studied here [see Table 1 for maximal uptakes]. Hence the extent of adsorption correlates

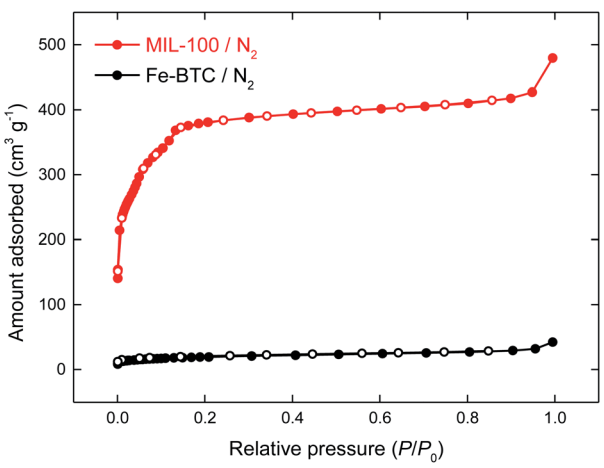

Fig. 3 Nitrogen adsorption (closed) and desorption (open) isotherms for MIL-100 (red) and Fe-BTC (black) at 77 K.

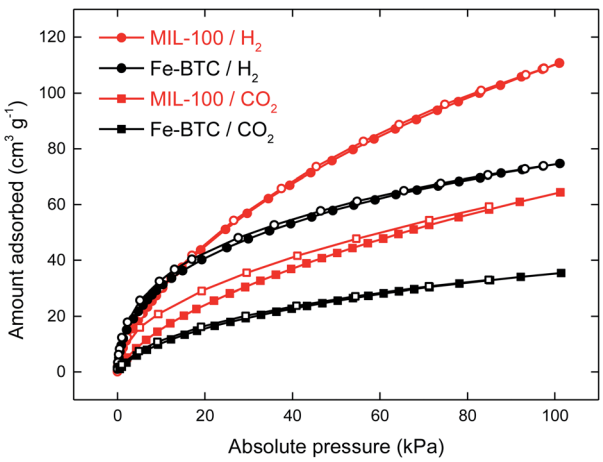

Fig. 4 Hydrogen at 77 K (circle) and carbon dioxide at 273 K (square) adsorption (closed) and desorption (open) isotherms for MIL-100 (red) and Fe-BTC (black).

Table 1 Maximal uptakes ($P/P_0 > 0.95$) by MIL-100 and Fe-BTC for the range of analytes

Analyte	Temperature (K)	MIL-100 ($cm^3\ g^{-1}$)	Fe-BTC ($cm^3\ g^{-1}$)
N_2	77	479.4	42.1
N_2	273	5.0	3.4
H_2	77	110.7	74.7
CO_2	273	64.4	35.4
CO_2	293	48.0	26.5
Xe	273	43.1	20.1
Ar	273	4.4	4.0
CH_4	273	10.8	10.6
CH_4	293	8.5	8.4
C_2H_4	273	63.0	32.5
C_2H_6	273	70.7	28.7
C_3H_6	273	147.4	44.0
C_3H_6	293	121.3	33.1
C_3H_8	273	141.7	18.8

with the guest molecule binding strength to the framework between 0 to 100 kPa.

Gas sorption of CO_2, with its highly polar bonding, is a simple way to probe a MOF's textural properties [Fig. 4]. MIL-100 displayed a maximal uptake of 64.4 $cm^3\ g^{-1}$ at 273 K, while Fe-BTC adsorbed 35.4 $cm^3\ g^{-1}$ in comparison. This further demonstrates that Fe-BTC is indeed capable of adsorption and is not dense, nor does it possess a collapsed porous interior. They both exhibited mild hysteresis upon desorption, indicating the adsorption and desorption branches are not in equilibrium.

The BET surface areas derived from these isotherms were 127 and 77 $m^2\ g^{-1}$ for MIL-100 and Fe-BTC, respectively [Table S4†].[41] These values represent the lower limit of accessible surface area, however they are nonetheless useful, comparative values given the limited utility of the N_2 isotherms at 77 K. These results are further diagnostic of activated diffusion occurring in Fe-BTC with the higher temperature of 273 K enabling diffusion of CO_2 through the structure. Hence, the ratio of maximal uptakes for CO_2 is more comparable to N_2 at 273 K than 77 K.

Additional isotherms of CO_2 were collected at 293 K for MIL-100 and Fe-BTC [Fig. S7 and S8†]. In both materials, the maximal uptake of CO_2 was reduced compared to that at 273 K. Virial analysis was carried out to determine the isosteric heat of adsorption, Q_{st}, for CO_2 [Fig. S9–S11 and Table S5†]. The Q_{st} at near-zero coverage was 23.8 kJ mol^{-1} for MIL-100, similar to previous reports, and 29.1 kJ mol^{-1} for Fe-BTC [Table 2].[18] This is consistent with stronger interactions occurring in Fe-BTC due to confinement of the CO_2 molecules within the smaller pore cavity compared to MIL-100. Q_{st} decreased at higher loadings of CO_2 in both materials.

Table 2 Isosteric heats of adsorption at near-zero coverage for MIL-100 and Fe-BTC

Analyte	MIL-100 (kJ mol^{-1})	Fe-BTC (kJ mol^{-1})
CO_2	23.8	29.1
CH_4	11.7	15.7
C_3H_6	41.4	—

Noble gases

Pure isotherms for Xe and Ar were measured at 273 K for MIL-100 and Fe-BTC [Fig. 5]. The Xe isotherm for MIL-100 was almost linear in the pressure range studied, with a maximal uptake of 43.1 $cm^3\ g^{-1}$, comparable to previous reports.[42] Fe-BTC had a maximal Xe uptake of 20.1 $cm^3\ g^{-1}$. The Xe isotherm for Fe-BTC began to plateau at higher pressures, indicating it was approaching saturation. Such behaviour is consistent with reduced pore space available in Fe-BTC compared to MIL-100. Fe-BTC displayed large hysteresis upon desorption, suggesting restricted diffusion of Xe through the structure, compared to the more accessible pores of MIL-100.

Both materials exhibited similar sorption of Ar, with near-linear adsorption and no hysteresis upon desorption. The maximal adsorption to MIL-100 was 4.4 $cm^3\ g^{-1}$ whilst Fe-BTC adsorbed 4.0 $cm^3\ g^{-1}$; these values are comparable to that of ZIF-8 and HKUST-1.[43] MIL-100 and Fe-BTC's maximal Ar uptakes are considerably lower than for Xe, which exhibits a greater van der Waals adsorption strength due to its higher boiling point and results in the hysteresis upon desorption for Fe-BTC. The smaller size of Ar enables easier diffusion through the structure leading to no hysteresis being observed.

Hydrocarbons

Gas sorption isotherms of five short-chain hydrocarbons (CH_4, C_2H_4, C_2H_6, C_3H_6 and C_3H_8) were collected at 273 K [Fig. 6 and 7]. In MIL-100, maximal uptakes at 100 kPa were primarily dictated by the hydrocarbon chain length (increasing C1 < C2 < C3) due to the higher boiling points of the longer chain molecules resulting in stronger adsorbate–adsorbent interactions. Conversely, Fe-BTC did not follow this trend, instead exhibiting some interesting adsorption behaviour.

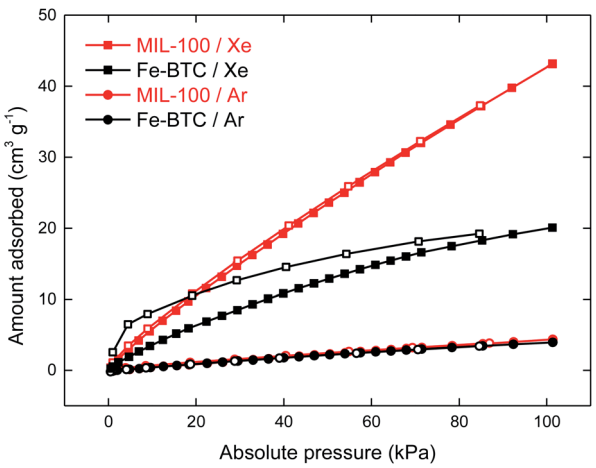

Fig. 5 Xenon (square) and argon (circle) adsorption (closed) and desorption (open) isotherms for MIL-100 (red) and Fe-BTC (black) at 273 K.

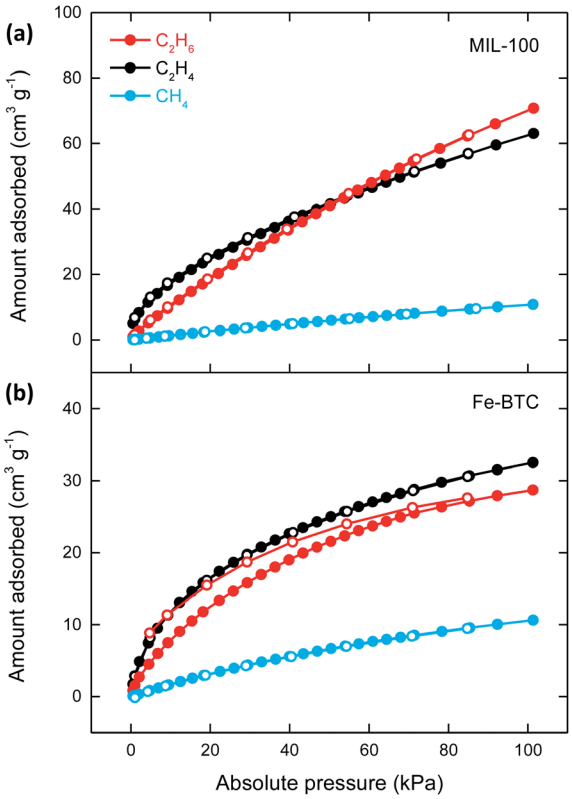

Fig. 6 Methane (blue), ethane (red) and ethene (black) adsorption (closed) and desorption (open) isotherms at 273 K for (a) MIL-100 and (b) Fe-BTC.

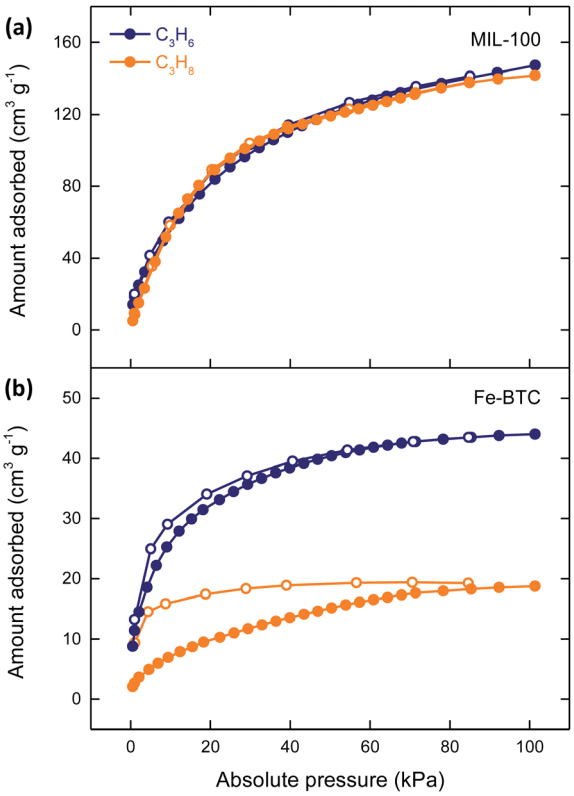

Fig. 7 Propene (navy) and propane (orange) adsorption (closed) and desorption (open) isotherms at 273 K for (a) MIL-100 and (b) Fe-BTC.

In both MIL-100 and Fe-BTC, CH_4 exhibited the lowest maximal uptake, adsorbing 10.8 and 10.6 cm^3 g^{-1}, respectively [Fig. 6a and b]. Neither material exhibited hysteresis and both isotherms were near-linear, together indicating that the pores were far from saturation. An additional isotherm of CH_4 was collected at 293 K for MIL-100 and Fe-BTC [Fig. S12 and S13†]. In both materials the maximal uptake of CH_4 was reduced at the higher temperature. Virial analysis revealed Q_{st} values at near-zero coverage of 11.7 and 15.7 kJ mol^{-1} for MIL-100 and Fe-BTC, respectively, again indicating weaker interactions between the adsorbate and MIL-100 [Fig. S14–16 and Table S6†]. Q_{st} values for CH_4 remained almost constant as the adsorbate loading increased.

In MIL-100, C_2H_4 exhibited steeper initial uptake than C_2H_6 up to 50 kPa [Fig. 6a]. As pressures increased, the C_2H_4 and C_2H_6 isotherms intersect and at 100 kPa the maximal uptake of C_2H_6 (70.7 cm^3 g^{-1}) was marginally higher than C_2H_4 (63.0 cm^3 g^{-1}). Neither gas displayed hysteresis upon desorption in MIL-100. This inability to discriminate between C_2H_4 and C_2H_6 is very common due to the similar physical properties of the two gases.[7] In Fe-BTC, C_2H_4 also showed steeper initial uptake than C_2H_6 at low pressure [Fig. 6b]. The maximal uptakes of C_2H_4 and C_2H_6 were 32.5 and 28.7 cm^3 g^{-1}, respectively. Upon desorption, Fe-BTC exhibited hysteresis with C_2H_6 but not C_2H_4. Under the activation conditions employed, there will be negligible unsaturated Fe(II) metal sites and hence π-back-bonding from the metal site to the π* orbital of the alkene will not be possible.[18] Instead, weaker interactions between the Lewis acidic Fe(III) metal sites that are present and the alkene will occur. These metal sites have a greater affinity towards the unsaturated molecule at low pressure causing the steeper initial adsorption of C_2H_4 in both materials.[18] C_2H_6 is only slightly larger than C_2H_4 (*ca.* 0.2 Å), and both have similar polarizability. Together this results in very similar maximal uptakes of C_2H_4 and C_2H_6 in both materials. However, the slightly larger size of C_2H_6 results in diffusion limitations through the disordered Fe-BTC structure. Hence, appreciable hysteresis is observed upon desorption of C_2H_6 in Fe-BTC, but not in the more accessible MIL-100 pore network.

The most interesting observations were made with the adsorption of C_3H_6 and C_3H_8. In MIL-100, C_3H_6 exhibited steeper initial uptake than C_3H_8 at low pressure [Fig. 7a]. At the highest pressure, the maximal uptakes of C_3H_6 (147.4 cm^3 g^{-1}) and C_3H_8 (141.7 cm^3 g^{-1}) were almost identical, and neither isotherm demonstrated hysteresis upon desorption, similar to previous reports.[44] Again, this inability to discriminate between C_3H_6 and C_3H_8 is very common amongst most MOFs.[7] Strikingly, Fe-BTC demonstrated very different sorption behaviour with a clear thermodynamic preference for C_3H_6 adsorption. The initial uptake was significantly steeper for C_3H_6 than C_3H_8, suggesting very different interactions upon initial adsorption. The maximal uptakes of C_3H_6 and C_3H_8 were 44.0 and 18.8 cm^3 g^{-1}, respectively, and both gases exhibited hysteresis upon desorption [Fig. 7b]. Unambiguous discrimination exists between the two

gases, with over twice the amount of C_3H_6 adsorbed than C_3H_8 in Fe-BTC. This level of discrimination is uncommon in the crystalline MOF domain and remains even rarer amongst disordered materials. Similar to C_2H_4, the steeper initial adsorption of C_3H_6 in both materials is due to interaction of the alkene with the Lewis acidic Fe(III) unsaturated metal sites and this effect appears more pronounced in Fe-BTC than in MIL-100. The marginally larger size and very similar polarizability of C_3H_8 compared to C_3H_6 has little effect in MIL-100, with near-identical maximal uptakes of the two gases. However, the disordered structure of Fe-BTC, predominantly containing the smaller pore cavity with a window aperture of only 5.5 Å, results in a pronounced magnification of the different physical properties of C_3H_6 and C_3H_8. This enables a significantly higher maximal uptake of C_3H_6, which can more freely occupy the pore space of Fe-BTC, at 100 kPa.

Motivated by these results, additional C_3H_6 isotherms were collected at 293 K [Fig. S17 and S18†]. Virial analysis of the adsorption branches of the isotherms revealed Q_{st} values at near-zero coverage of 41.4 kJ mol^{-1} for MIL-100 [Fig. S19, & S20 and Table S7†]. Unfortunately, due to the pronounced hysteresis observed for Fe-BTC, virial analysis could not be performed with any degree of certainty.

We measured the kinetics of C_3H_8 and C_3H_6 adsorption by MIL-100 and Fe-BTC to investigate differences in the rates of gas uptake [Fig. 8]. In MIL-100, we observed rapid adsorption kinetics for both gases with C_3H_8 reaching saturation in less than one minute and C_3H_6 is just over two minutes. This is due to the large pores and apertures enabling unhindered diffusion through MIL-100's structure. Fe-BTC exhibited significantly slower uptake compared to MIL-100, C_3H_8 reaching saturation after 26 minutes and C_3H_6 after 76 minutes. The slower diffusion of both gases in Fe-BTC is consistent with our structural model of this material, which contains tortuous diffusion pathways with bottlenecks and apertures that are comparable to the kinetic diameters of C_3H_8 and C_3H_6. The more pronounced hysteresis in the C_3H_8 isotherm of Fe-BTC compared to C_3H_6 appears not to arise from a difference in diffusion rates between these two gases. Instead, we speculate that propane induces a subtle structural transformation of the framework upon adsorption.[45]

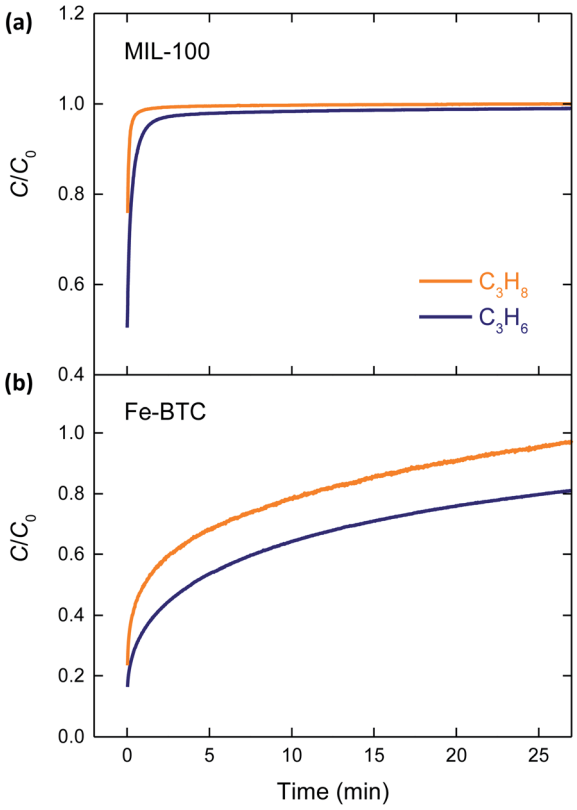

Fig. 8 Kinetic profiles for the uptake of propane (orange) and propene (navy) by (a) MIL-100 and (b) Fe-BTC. The final propane pressures were 53.5 and 31.8 kPa for MIL-100 and Fe-BTC, respectively. The final propene pressures were 51.6 and 21.7 kPa for MIL-100 and Fe-BTC, respectively.

Thermodynamic gas selectivity

The topological disorder in Fe-BTC has a large impact on its adsorption properties. Given the technical challenges associated with measuring adsorption isotherms of gaseous mixtures, ideal adsorbed solution theory (IAST) was employed to quantify the thermodynamic gas selectivities in MIL-100 and Fe-BTC.[46,47] Specifically, the selectivities towards 50 : 50 binary mixtures of CO_2/N_2, CH_4/N_2 and CO_2/CH_4 were investigated at 273 K. These mixtures are industrially relevant for the processing of flue gases, biogas purification, and natural gas purification.[46] Initially, each pure-component adsorption isotherm was fitted to one of four models before being used to calculate the thermodynamic selectivities of MIL-100 and Fe-BTC [see ESI Methods & Fig. S21 & Table S8†].

In MIL-100, the CO_2/N_2 selectivity was 55.7 at 1 kPa, which increased by a factor of 2.5 to 139.7 at 100 kPa, while Fe-BTC had an initial selectivity of 67.8 that increased by a factor of almost 2.6 to 174.8 at 100 kPa [Fig. 9a]. This favourable adsorption of CO_2 over N_2 relates to the activated diffusion phenomenon discussed previously and the reduced impact of the molecular sieving effect experienced by CO_2. Our results for MIL-100 are approximately four times higher than that previously reported; however, this is likely due to the lower experimental temperatures used here.[46]

The adsorption of CH_4 and N_2 is equally competitive, and the resulting selectivity was an order of magnitude smaller than for CO_2/N_2 [Fig. 9b]. The CH_4/N_2 selectivity for MIL-100 was 3.3 at 1 kPa and 2.5 at 100 kPa, while Fe-BTC was 7.2 at 1 kPa and 5.0 at 100 kPa. Neither material exhibited pressure dependence.

The CO_2/CH_4 selectivity for MIL-100 was 21.8 at 1 kPa and 17.4 at 100 kPa, consistent with previous reports [Fig. 9c].[46] Fe-BTC had a CO_2/CH_4 selectivity of 12.8 at 1 kPa and 11.7 at 100 kPa. Again, neither material showed significant pressure dependence. The slightly enhanced selectivity in MIL-100 is consistent with the larger, relative Q_{st} value derived for CO_2 with respect to CH_4 for MIL-100 compared to Fe-BTC, which results from the large quadrupole moment of CO_2.

Due to the adsorption and desorption branches of Fe-BTC's C_3H_6 isotherm not being at equilibrium, we were unable to perform IAST analysis on these data to examine its thermodynamic selectivity towards C_3H_6/C_3H_8 mixtures.

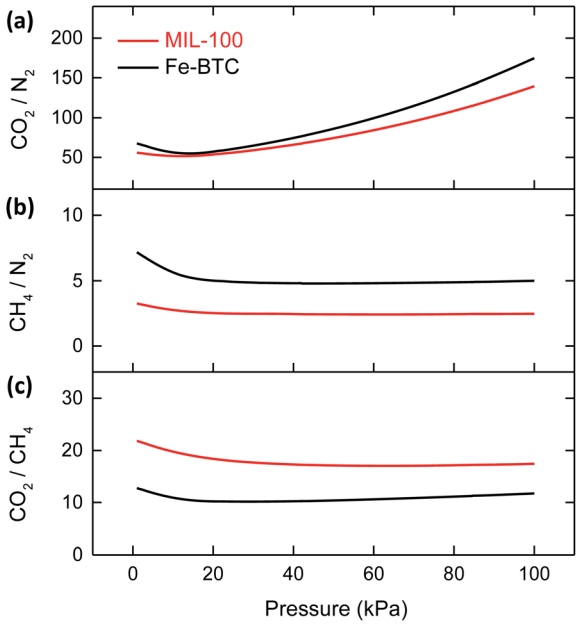

Fig. 9 Thermodynamic selectivities of MIL-100 (red) and Fe-BTC (black) towards 50 : 50 binary mixtures of (a) CO_2/N_2, (b) CH_4/N_2 and (c) CO_2/CH_4 calculated from single-component adsorption isotherms using the IAST method.

Conclusions

As perhaps anticipated, the giant pore architecture and high porosity of crystalline MIL-100 mean that it exhibits a higher maximal uptake for many gases compared to its disordered counterpart, Fe-BTC. However, the absence of long-range order in the disordered material affects higher affinity towards certain gases, such as CO_2 and CH_4. It also leads to the emergence of highly sought after C_3H_6/C_3H_8 discrimination capabilities and highlights the prospective utility of disordered MOFs in the field of gas sorption and separation.

Critically, our study has established that while the ordered nature of MIL-100 facilitates accessibility to the larger internal pore network, the presence of substantial structural disorder, as in Fe-BTC, may impart powerful separation abilities on the framework. The balance between order and disorder in MOFs as a route to augment their sorption properties is an appealing avenue for future investigation. Two potential routes to tune the interplay between selectivity and capacity in these materials include (i) the progressive incorporation of defects into MIL-100 to introduce disorder or (ii) adjusting the synthesis of Fe-BTC to retain a greater degree of porosity.

The number of disordered, functional MOF structures is rapidly growing.[48] While we have used the MIL-100 and Fe-BTC pairing here as an important demonstration that structural disorder can enhance the gas sorption properties of MOFs, we are certain that this behaviour extends to many more of these disordered materials. The use of structural disorder within MOFs as a tool to enhance gas storage and separation abilities remains widely underappreciated, which we believe hinders the realisation of the full potential of this fascinating class of materials.

Author contributions

A. F. S. designed the project. S. G. T. and T. D. B. supervised the project. A. F. S. synthesised the samples and collected the powder X-ray diffraction data. C. W. A., L. K. M. and S. J. L. collected the gas sorption data. A. F. S. analysed the data with the help of S. G. T. A. F. S. wrote the manuscript with the input of all authors.

Conflicts of interest

T. J. works for Johnson Matthey PLC, a company with an interest in the commercialisation of MOF materials.

Acknowledgements

A. F. S. acknowledges the EPSRC for a PhD studentship award under the industrial CASE scheme, along with Johnson Matthey PLC (JM11106). C.W.A. acknowledges the Royal Society for a PhD studentship (RG160498) and the Commonwealth Scientific and Industrial Research Council for additional support (C2017/3108). S.G.T. acknowledges the MacDiarmid Institute, RSNZ Marsden Fund (14-MAU-024) for financial support. T.D.B. acknowledges the Royal Society for a University Research Fellowship (UF150021), the Leverhulme Trust for a Philip Leverhulme Prime, and the University of Canterbury Te Whare Wānanga o Waitaha, New Zealand, for a University of Cambridge Visiting Canterbury Fellowship. T.D.B. and S.G.T. acknowledge the Royal Society of New Zealand (RSNZ) Catalyst fund (18-MAU-022-CSG) for financial support.

Notes and references

1 J. R. Long and O. M. Yaghi, *Chem. Soc. Rev.*, 2009, **38**, 1213–1214.
2 O. K. Farha, I. Eryazici, N. C. Jeong, B. G. Hauser, C. E. Wilmer, A. A. Sarjeant, R. Q. Snurr, S. T. Nguyen, A. Ö. Yazaydin and J. T. Hupp, *J. Am. Chem. Soc.*, 2012, **134**, 15016–15021.
3 M. Hirscher, B. Panella and B. Schmitz, *Microporous Mesoporous Mater.*, 2010, **129**, 335–339.
4 D. S. Sholl and R. P. Lively, *Nature*, 2016, **532**, 435–437.
5 J. R. Li, R. J. Kuppler and H. C. Zhou, *Chem. Soc. Rev.*, 2009, **38**, 1477–1504.
6 R. B. Lin, S. Xiang, H. Xing, W. Zhou and B. Chen, *Coord. Chem. Rev.*, 2019, **378**, 87–103.
7 Z. Bao, G. Chang, H. Xing, R. Krishna, Q. Ren and B. Chen, *Energy Environ. Sci.*, 2016, **9**, 3612–3641.
8 M. S. Denny, J. C. Moreton, L. Benz and S. M. Cohen, *Nat. Rev. Mater.*, 2016, **1**, 1–17.
9 W. J. Koros and C. Zhang, *Nat. Mater.*, 2017, **16**, 289–297.
10 Y. Gurdal and S. Keskin, *Ind. Eng. Chem. Res.*, 2012, **51**, 7373–7382.
11 D. Liu and C. Zhong, *J. Mater. Chem.*, 2010, **20**, 10308–10318.

12 Z. Li, P. Liu, C.-J. C. Ou and X. Dong, *ACS Sustainable Chem. Eng.*, 2020, **8**, 15378–15404.
13 B. Liang, X. Zhang, Y. Xie, R. Lin, R. Krishna, H. Cui, Z. Li, Y. Shi, H. Wu, W. Zhou and B. Chen, *J. Am. Chem. Soc.*, 2020, **142**, 17795–17801.
14 O. T. Qazvini, R. Babarao and S. G. Telfer, *Nat. Commun.*, 2021, **12**, 1–8.
15 O. T. Qazvini and S. G. Telfer, *ACS Appl. Mater. Interfaces*, 2021, **13**, 12141–12148.
16 L. K. Macreadie, R. Babarao, C. J. Setter, S. J. Lee, O. T. Qazvini, A. J. Seeber, J. Tsanaktsidis, S. G. Telfer, S. R. Batten and M. R. Hill, *Angew. Chem., Int. Ed.*, 2020, **59**, 6090–6098.
17 P. Horcajada, S. Surblé, C. Serre, D. Y. Hong, Y. K. Seo, J. S. Chang, J. M. Grenèche, I. Margiolaki and G. Férey, *Chem. Commun.*, 2007, 2820–2822.
18 J. W. Yoon, Y. K. Seo, Y. K. Hwang, J. S. Chang, H. Leclerc, S. Wuttke, P. Bazin, A. Vimont, M. Daturi, E. Bloch, P. L. Llewellyn, C. Serre, P. Horcajada, J. M. Grenèche, A. E. Rodrigues and G. Férey, *Angew. Chem., Int. Ed.*, 2010, **49**, 5949–5952.
19 J. W. Yoon, J. S. Lee, S. Lee, K. H. Cho, Y. K. Hwang, M. Daturi, C. H. Jun, R. Krishna and J. S. Chang, *Chem.–Eur. J.*, 2015, **21**, 18431–18438.
20 S. Wuttke, P. Bazin, A. Vimont, C. Serre, Y. K. Seo, Y. K. Hwang, J. S. Chang, G. Férey and M. Daturi, *Chem.–Eur. J.*, 2012, **18**, 11959–11967.
21 G. Zhong, D. Liu and J. Zhang, *Cryst. Growth Des.*, 2018, **18**, 7730–7744.
22 T. D. Bennett and A. K. Cheetham, *Acc. Chem. Res.*, 2014, **47**, 1555–1562.
23 T. D. Bennett and S. Horike, *Nat. Rev. Mater.*, 2018, **3**, 431–440.
24 W. Xiang, Y. Zhang, Y. Chen, C. Liu and X. Tu, *J. Mater. Chem. A*, 2020, **8**, 21526–21546.
25 T. D. Bennett, Y. Yue, P. Li, A. Qiao, H. Tao, N. G. Greaves, T. Richards, G. I. Lampronti, S. A. T. Redfern, F. Blanc, O. K. Farha, J. T. Hupp, A. K. Cheetham and D. A. Keen, *J. Am. Chem. Soc.*, 2016, **138**, 3484–3492.
26 Q. Ma, H. Jin and Y. Li, *Chem.–Eur. J.*, 2020, **26**, 13137–13141.
27 S. Cao, T. D. Bennett, D. A. Keen, A. L. Goodwin and A. K. Cheetham, *Chem. Commun.*, 2012, **48**, 7805–7807.
28 M. R. Lohe, M. Rose and S. Kaskel, *Chem. Commun.*, 2009, 6056–6058.
29 A. F. Sapnik, I. Bechis, S. M. Collins, D. N. Johnstone, G. Divitini, A. J. Smith, P. A. Chater, M. A. Addicoat, T. Johnson, D. A. Keen, K. E. Jelfs and T. D. Bennett, *Nat. Commun.*, 2020, **12**, 1–15.
30 L. Sciortino, A. Alessi, F. Messina, G. Buscarino and F. M. Gelardi, *J. Phys. Chem. C*, 2015, **119**, 7826–7830.
31 A. Dhakshinamoorthy, M. Alvaro, P. Horcajada, E. Gibson, M. Vishnuvarthan, A. Vimont, J. M. Grenèche, C. Serre, M. Daturi and H. Garcia, *ACS Catal.*, 2012, **2**, 2060–2065.
32 A. Dhakshinamoorthy, M. Alvaro and H. Garcia, *Chem. Commun.*, 2012, **48**, 11275–11288.
33 A. F. Sapnik, D. N. Johnstone, S. M. Collins, G. Divitini, A. M. Bumstead, C. W. Ashling, P. A. Chater, T. Johnson, D. A. Keen and T. D. Bennett, *Dalton Trans.*, 2021, **50**, 5011–5022.
34 M. Rivera-Torrente, M. Filez, R. Hardian, E. Reynolds, B. Seoane, M. V. Coulet, F. E. Oropeza Palacio, J. P. Hofmann, R. A. Fischer, A. L. Goodwin, P. L. Llewellyn and B. M. Weckhuysen, *Chem.–Eur. J.*, 2018, **24**, 7498–7506.
35 K. Guesh, C. A. D. Caiuby, Á. Mayoral, M. Díaz-García, I. Díaz and M. Sanchez-Sanchez, *Cryst. Growth Des.*, 2017, **17**, 1806–1813.
36 Y. K. Seo, J. W. Yoon, J. S. Lee, U. H. Lee, Y. K. Hwang, C. H. Jun, P. Horcajada, C. Serre and J. S. Chang, *Microporous Mesoporous Mater.*, 2012, **157**, 137–145.
37 A. A. Coelho, *TOPAS-Academic, version 6 (computer software), Tech. Rep.*, Coelho Software, Brisbane.
38 L. Frentzel-Beyme, M. Kloß, P. Kolodzeiski, R. Pallach and S. Henke, *J. Am. Chem. Soc.*, 2019, **141**, 12362–12371.
39 H. De Jonge and M. C. Mittelmeijer-Hazeleger, *Environ. Sci. Technol.*, 1996, **30**, 408–413.
40 M. Latroche, S. Surblé, C. Serre, C. Mellot-Draznieks, P. L. Llewellyn, J.-H. Lee, J.-S. Chang, S. H. Jhung and G. Férey, *Angew. Chem.*, 2006, **118**, 8407–8411.
41 K. C. Kim, T. U. Yoon and Y. S. Bae, *Microporous Mesoporous Mater.*, 2016, **224**, 294–301.
42 S. J. Lee, T. U. Yoon, A. R. Kim, S. Y. Kim, K. H. Cho, Y. K. Hwang, J. W. Yeon and Y. S. Bae, *J. Hazard. Mater.*, 2016, **320**, 513–520.
43 M. V. Parkes, C. L. Staiger, J. J. Perry IV, M. D. Allendorf and J. A. Greathouse, *Phys. Chem. Chem. Phys.*, 2013, **15**, 9093–9106.
44 A. R. Kim, T. U. Yoon, E. J. Kim, J. W. Yoon, S. Y. Kim, J. W. Yoon, Y. K. Hwang, J. S. Chang and Y. S. Bae, *Chem. Eng. J.*, 2018, **331**, 777–784.
45 H. Wu, C. G. Thibault, H. Wang, K. A. Cychosz, M. Thommes and J. Li, *Microporous Mesoporous Mater.*, 2016, **219**, 186–189.
46 P. Billemont, N. Heymans, P. Normand and G. De Weireld, *Adsorption*, 2017, **23**, 225–237.
47 N. F. Cessford, N. A. Seaton and T. Düren, *Ind. Eng. Chem. Res.*, 2012, **51**, 4911–4921.
48 R. Thyagarajan and D. S. Sholl, *Chem. Mater.*, 2020, **32**, 8020–8033.